Cryo-EM structure of the NLRC4^{CARD} filament provides insights into how symmetric and asymmetric supramolecular structures drive inflammasome assembly

Received for publication, October 1, 2018, and in revised form, October 26, 2018 Published, Papers in Press, November 1, 2018, DOI 10.1074/jbc.RA118.006050

Mariusz Matyszewski[‡1], **Weili Zheng**[§1], **Jacob Lueck**[‡], **Brendan Antiochos**[¶], **Edward H. Egelman**[§2], **and Jungsan Sohn**[‡3]

From the [‡]*Department of Biophysics and Biophysical Chemistry, Johns Hopkins University School of Medicine, Baltimore, Maryland 21205,* [§]*Department of Biochemistry and Molecular Genetics, University of Virginia School of Medicine, Charlottesville, Virginia 22908, and* [¶]*Division of Rheumatology, Johns Hopkins University School of Medicine, Baltimore, Maryland 21205*

Edited by Ruma Banerjee

Inflammasomes are supramolecular signaling platforms integral to innate immune defense against invading pathogens. The NOD-like receptor (NLR) family apoptosis inhibitory protein (NAIP)·NLR family caspase-recruiting domain (CARD) domain-containing 4 (NLRC4) inflammasome recognizes intracellular bacteria and induces the polymerization of the caspase-1 protease, which in turn executes maturation of interleukin-1β (IL-1β) and pyroptosis. Several high-resolution structures of the fully assembled NAIP·NLRC4 complex are available, but these structures do not resolve the architecture of the CARD filament in atomic detail. Here, we present the cryo-EM structure of the filament assembled by the CARD of human NLRC4 (NLRC4^{CARD}) at 3.4 Å resolution. The structure revealed that the helical architecture of the NLRC4^{CARD} filament is essentially identical to that of the downstream filament assembled by the CARD of caspase-1 (casp1^{CARD}), but deviates from the split washer-like assembly of the NAIP·NLRC4 oligomer. Our results suggest that architectural complementarity is a major driver for the recognition between upstream and downstream CARD assemblies in inflammasomes. Furthermore, a Monte Carlo simulation of the NLRC4^{CARD} filament assembly rationalized why an (un)decameric NLRC4 oligomer is optimal for assembling the helical base of the NLRC4^{CARD} filament. Together, our results explain how symmetric and asymmetric supramolecular assemblies enable high-fidelity signaling in inflammasomes.

This work was supported by Research Scholars Grant RG-15–224 from American Cancer Society (to J. S.), National Institutes of Health Grant R35GM0352569 (to E. H. E.), and Rheumatology Research Foundation and Cupid Foundation (to B.A.). The authors declare that they have no conflicts of interest with the contents of this article. The content is solely the responsibility of the authors and does not necessarily represent the official views of the National Institutes of Health.

This article contains Fig. S1.

The atomic coordinates and structure factors (code 6MKS) have been deposited in the Protein Data Bank (http://wwpdb.org/).

The corresponding cryo-EM map was deposited in the Electron Microscopy Data Bank with accession code EMD-9137.

[1] Both authors contributed equally to this work.

[2] To whom correspondence may be addressed. E-mail: egelman@virginia.edu.

[3] To whom correspondence may be addressed. E-mail: jsohn@jhmi.edu.

Inflammasomes are supramolecular signaling platforms integral to the metazoan innate immune system (1). The outcome of inflammasome pathways is the activation of the caspase-1 protease, which executes two key innate immune processes (1). First, caspase-1 cleaves pro–IL-1β into mature IL-1β (2), and second, the protease activates pore-forming gasdermin-D, which provides the secretory channel to IL-1β and also promotes pyroptosis (3). Inflammasomes are essential for host defense against pathogen invasion (*e.g.* HIV, Herpesviridae, *Listeria monocytogene*, and *Francisella tularemia*) (4–8). Moreover, they are implicated in regulating various human maladies (*e.g.* rheumatoid arthritis and systemic lupus erythematosus (9, 10), sepsis (11), metabolic disorders (12, 13), and various types of cancer (14, 15)).

The vast majority of inflammasome receptors such as AIM2 and NLRP3 signal through ASC (Fig. 1*A*, *left*); AIM2, absent in melanoma 2; NLRP3, nucleotide-binding oligomerization domain (NOD)-like receptor (NLR) containing pyrin-domain (PYD) 3; ASC, apoptosis-associated speck-forming protein containing CARD (1). That is, incoming signals induce oligomerization of upstream receptors, resulting in filament assembly of their PYDs (16). Upstream PYD filaments then nucleate the polymerization of ASC^{PYD} (PYD of ASC), dramatically accelerating the assembly of the downstream filament (16, 17)). The ASC^{PYD} filament in turn promotes the filament assembly of its CARD (ASC^{CARD}) (16, 18), which then nucleates the filament assembly of the CARD of caspase-1 (casp1^{CARD}). This final polymerization step activates the protease via proximity-induced dimerization and auto-proteolysis (1, 16, 18). However, not all inflammasome receptors require ASC to activate caspase-1. Most notably, the NAIP-NLRC4 signaling axis represents a unique ASC-independent pathway (19) (Fig. 1, *A* and *B*, NAIP, NLRC4). For instance, NAIP directly recognizes bacterial rod proteins such as PrgJ and FliC, subsequently undergoing a conformational change from a closed inactive state to an active open state (20–24). Activated NAIP then nucleates the oligomerization of NLRC4, resulting in a split washer-like structure composed of 10 to 11 NLRC4 subunits (20–24) (Fig. 1, *A* and *B*). This oligomerization allows NLRC4^{CARD} to cluster into a helical filament at the center, providing a scaffold for the assembly of casp1^{CARD} filament (23, 24) without requiring ASC (19) (Fig. 1, *A* and *B*).

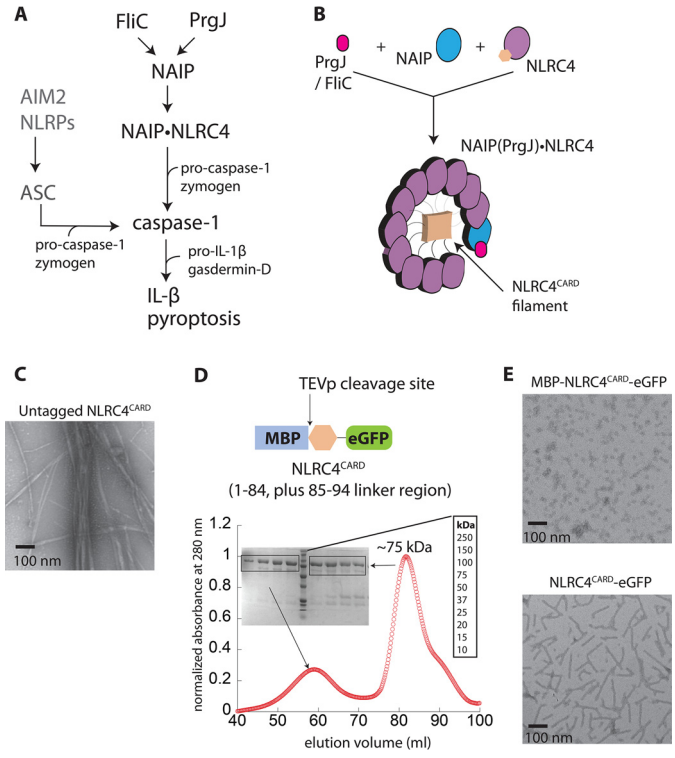

Figure 1. Preparation of the NLRC4^{CARD} for cryo-EM reconstruction. *A*, a scheme describing inflammasome signaling pathways. *B*, a cartoon describing the assembly of the NAIP•NLRC4 complex. Upon binding of bacterial proteins, NAIP undergoes a conformational change and consequently nucleates the assembly of (un)decameric NLRC4 oligomer that resembles a split washer. *C*, nsEM micrographs showing the filament assembly by NLRC4^{CARD} constructs. *D*, *top*, a scheme describing the NLRC4^{CARD} construct used for cryo-EM reconstruction. *Bottom*, SEC (Superdex 200 16/600) and SDS-PAGE of MBP-NLRC4^{CARD}-eGFP. *E*, nsEM micrographs showing the filament assembly by NLRC4^{CARD}-eGFP.

Currently, multiple near-atomic resolution structures of the fully assembled NAIP•NLRC4 complex are available (21–24). However, these structures either omit or fail to resolve the architecture of the CARD filament in atomic detail. Such a gap in knowledge leaves two key questions unanswered in understanding the mechanisms by which the NAIP•NLRC4 inflammasome operates: What is the structural framework that allows NLRC4 to recognize caspase-1, and why is the split washer-like assembly composed of 10 to 11 NLRC4 subunits necessary to assemble the CARD filament?

Here, we present the cryo-EM structure of NLRC4^{CARD} filament at 3.4 Å resolution, which is a 1-start, left-handed helix with 3.6 subunits per helical turn. The overall architecture of the NLRC4^{CARD} filament is remarkably similar to that of the casp1^{CARD} filament (18), indicating that the CARD•CARD interaction between upstream NLRC4 and downstream caspase-1 is based on congruent helical assemblies. Side-chains that mediate filament assembly are also similar between casp1^{CARD} and NLRC4^{CARD}, indicating that conserved interactions underpin the assembly of homologous suprastructures. A Monte Carlo simulation of the CARD filament assembly suggests that the (un)decameric assembly of the NLRC4 oligomer maximizes the probability of assembling the helical base of the NLRC4^{CARD} filament, which provides the cognate signaling interface for caspase-1. Together, our studies provide insights into how symmetric and asymmetric supramolecular structures might maximize the signal efficiency and fidelity in inflammasome pathways.

Results

Preparation of the NLRC4^{CARD} filament for structural studies

NAIP and NLRC4 co-assemble into a split washer-like structure in which NLRC4^{CARD} clusters into a helical filament in the middle (21–24) (Fig. 1*B*). To understand the architectural organization of the NLRC4^{CARD} filament, we generated C-terminally His$_6$-tagged NLRC4^{CARD}. The size-exclusion chromatography (SEC)[4] profile during purification indicated that this construct behaves as multiple oligomeric species (Fig. S1*A*). Moreover, negative stain EM (nsEM) imaging revealed that NRLC4^{CARD} self-assembles into filaments (Fig. 1*C*). Our results support the notion that monomeric NLRC4 assumes a closed conformation to suppress the self-polymerization activity of its CARD (20). Nevertheless, this construct was not conducive to structural studies, as the filaments were prone to aggregation and bundling (Fig. 1*C*).

While screening for a more suitable sample for structural studies, we found an NLRC4^{CARD} construct with an N-terminal maltose-binding protein (MBP) and a C-terminal enhanced green fluorescence protein (eGFP) to be an ideal candidate for structural determination (Fig. 1*D*, *top*). For instance, the resulting protein purified mostly as a monomer with some oligomeric fraction (likely a dimer) (Fig. 1*D*). Under nsEM, the sample showed nonfilamentous oligomers, and cleaving MBP using the tobacco etch virus protease (TEVp) induced filament assembly (Fig. 1*E*). Importantly, it appeared that the presence of C-terminal eGFP greatly reduced the aggregation of NLRC4^{CARD} filaments (Fig. 1, *C versus E*). These observations indicated that using N- and C-terminal protein tags helps control the oligomerization activity of NLRC4^{CARD}, resulting in a suitable sample for cryo-EM reconstruction.

Cryo-EM reconstruction of the NLRC4^{CARD} filament

To determine the architecture of the NLRC4^{CARD} filament, we collected the cryo-EM images of NLRC4^{CARD}-eGFP filaments (Fig. 2*A*). The average power spectrum of the 384-pixel-long overlapping filament segments showed that the NLRC4^{CARD} filament displays a one-start helical symmetry of 100.6° rotation (3.6 subunit per helical turn) and an axial rise of 5.0 Å (Fig. 2*B*). The ~3.4 Å resolution of the reconstruction allowed for an unambiguous determination of the hand of the structure. The reconstruction showed that the one-start helix must be left-handed, as this yielded clearly right-handed α-helices. The alternative reconstruction, assuming that the one-start helix is right-handed, yielded left-handed α-helices, which would be impossible for a protein. (Fig. 2*D*). Of note, these parameters are remarkably consistent with other CARD filaments such as casp1^{CARD} (100.21° and 5.1 Å) (18), MAVS^{CARD} (mitochondria antiviral signaling protein; 101.1° and 5.13Å) (25), and BCL10^{CARD} (B-cell lymphoma 10; 100.8° and 5.1 Å) (26) filaments. Our observations not only highlight the shared

[4] The abbreviations used are: SEC, size-exclusion chromatography; nsEM, negative stain EM; eGFP, enhanced GFP; TEVp, tobacco etch virus protease; CTF, contrast transfer function; FSC, Fourier Shell Correlation.

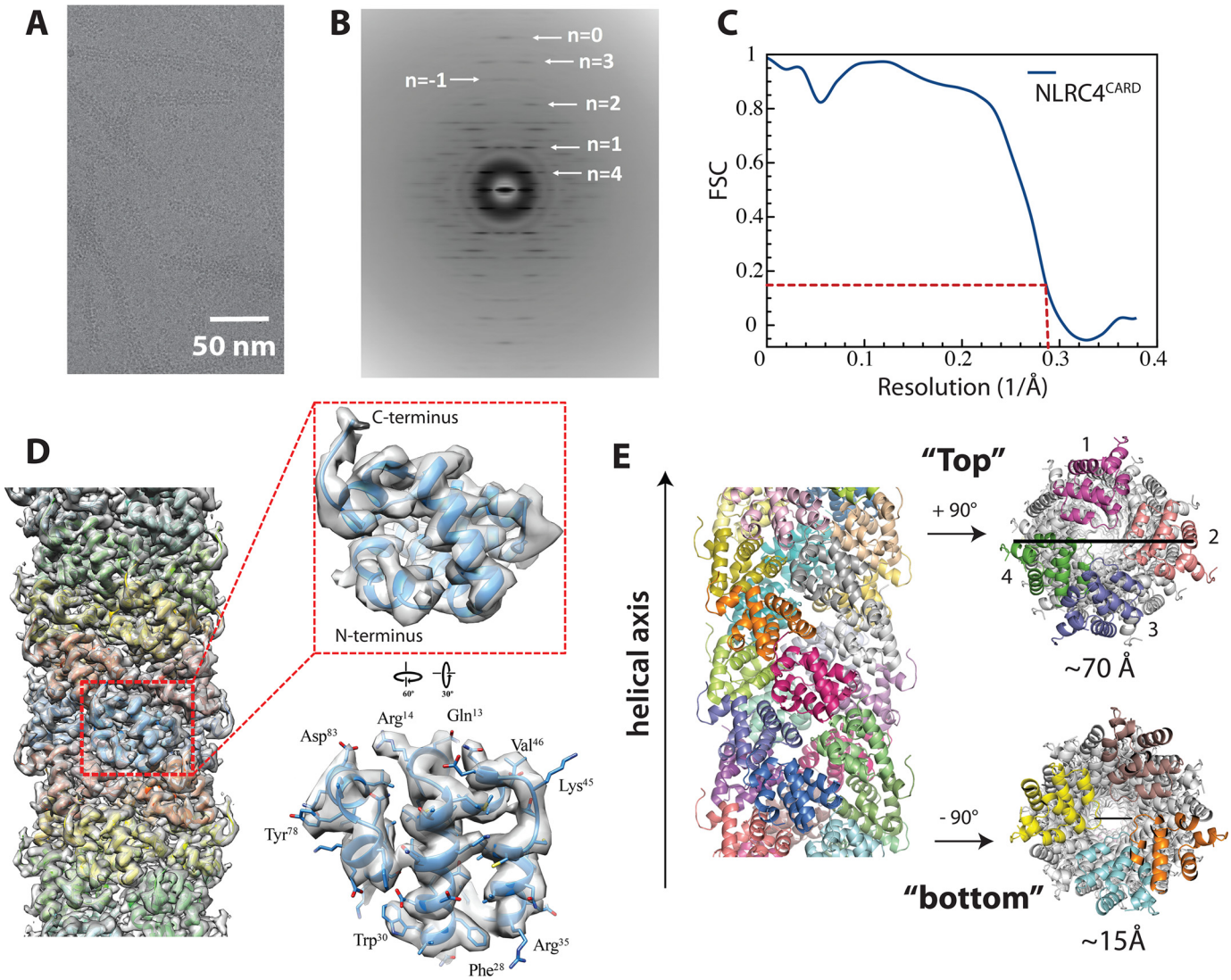

Figure 2. The cryo-EM structure of NLRC4^{CARD}. *A*, a cryo-electron micrograph of NLRC4^{CARD}-eGFP filaments. *B*, an average power spectrum of the NLRC4^{CARD}-eGFP filament generated from 299,537 overlapping segments. *C*, the FSC curve of the cryo-EM map of the NLRC4^{CARD} filament obtained from 299,537 segments. The *dotted lines* indicate the 0.143 threshold for the resolution. *D*, the NLRC4^{CARD} filament model docked into the EM map. The monomer with visible side-chains is also shown. *E*, the model of NLRC4^{CARD} filament. In the *top* and *bottom* views, the chains (subunits) located at either pole are colored differently from the rest of the filament. The *numbers* indicate the four subunits that compose the horizontal plane of the filament.

assembly theme among CARD suprastructures but also indicate that our reconstruction represents a biologically relevant assembly. The resolution of the final model was 3.4 Å according to the gold standard method (Fig. 2*C* and Fig. S1*B*). The high-resolution map then allowed us to model in most bulky and aliphatic side-chains (Fig. 2*D*). Of note, the C-terminal eGFP was not visible in our reconstruction, indicating that the tag is flexibly attached to the filament and does not prevent polymerization (Fig. 2*D*). The final model showed that four NLRC4^{CARD} protomers constitute the base of the filament (*i.e.* 3.6 subunits per helical turn) (Fig. 2*E*). The diameter of the outer rim is about 70 Å and that of the inner cavity is about 15 Å (Fig. 2*E*).

As seen from other CARD filaments (18, 25, 26), our structure showed that each NLRC4^{CARD} subunit contributes six unique surfaces to filament assembly, resulting in three distinct interfaces (Fig. 3*A*). Examining each interface of the filament indicated that the type 1a:1b interface is largely mediated by salt bridges and polar interactions (Fig. 3*B*). On the other hand, the type 2a:2b and 3a:3b interfaces are mediated by both polar and hydrophobic interactions (Fig. 3*B*). Aligning the NLRC4^{CARD} filament to the casp1^{CARD} filament revealed remarkable structural similarity between the upstream and downstream assemblies with all subunits placed in nearly identical positions along the helical axis (Fig. 3*C*). Such near perfect architectural complementarity supports the notion that upstream oligomers provide templates for assembling downstream oligomers in signaling supramolecular structures (25, 27, 28).

Conserved side-chain interactions underpin the assembly of homologous filaments

Each NLRC4^{CARD} subunit makes the three unique interactions in the filament (Fig. 3, *A–C*), using the same interface pairs as in the casp1^{CARD} filament (18). Moreover, we noted that the interface residues are similar between the upstream and downstream proteins (Fig. 3*D*). To determine the energetic con-

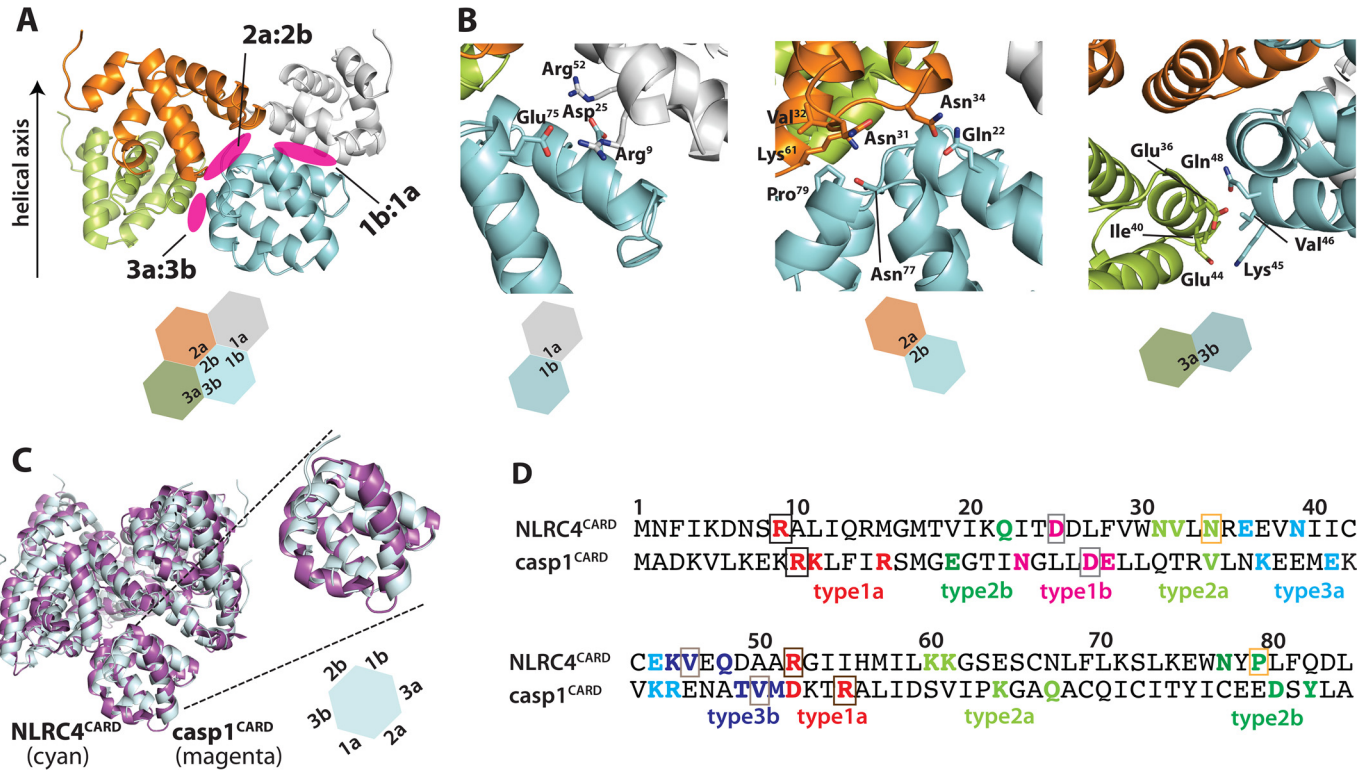

Figure 3. Deciphering NLRC4^{CARD} side-chains that mediate three unique filament interfaces. *A*, a cartoon representation of three unique filament interfaces and "type" of participating surfaces per subunit. *B*, side-chains that mediate each unique protein-protein interactions around each filament interface are shown as a *stick* configuration. *C*, an overlay of the NLRC4^{CARD} and casp1^{CARD} (PDB ID: 5FNA) filaments. The root mean square deviation of aligned chain A is 1.2 Å. The hexagon representing a NLRC4^{CARD} subunit is shown with six unique protein-protein interaction surfaces following the convention used in Ref. 18. *D*, an amino acid sequence alignment of NLRC4^{CARD} and casp1^{CARD}. Side-chains that participate in each filament interface is indicated. *Boxed* side-chains indicate those we mutated, and equivalent caspase-1 residues are also *boxed* with the same color. Asn-34 (*N*) and Pro-70 (*P*) are unique to NLRC4 (colored in *light orange*).

tribution of NLRC4^{CARD} side-chains in assembly, we mutated several conserved and unconserved side-chains on each of three unique interfaces and tested whether they compromise the filament assembly of NLRC4^{CARD}-eGFP *in vitro* and also in cells (Fig. 4; see also Fig. 3, *C* and *D*, for their positions). All NLRC4^{CARD} mutants purified predominantly as monomers (Fig. 4*A*) and did not show any significant oligomers under nsEM (Fig. S1*C*). Upon cleaving MBP via TEVp, most mutants did not produce filaments (only P79R showed filaments, but much less than WT) (Fig. 4*B*). These observations indicated that mutations compromised the oligomerization activity of NLRC4^{CARD}. To establish the physiological relevance of our *in vitro* studies, we also transfected WT and mutant NLRC4^{CARD}-eGFP into HEK293T cells and monitored the filament assembly via confocal microscopy. WT NLRC4^{CARD}-eGFP showed filaments in cells (Fig. 4, *C* and *D*). No filaments were observed from R52E and D25R, and significantly fewer filaments were detected from the rest of the mutants (Figs. 4, *C* and *D*). Overall, our *in vitro* and cell-based experiments consistently agree with our reconstruction, and also suggest that conserved side-chain interactions in CARD filaments underpin their common helical architecture.

Asymmetric assembly between the NLRC4^{CARD} filament and NAIP·NLRC4 oligomer

The congruent architecture between the NLRC4^{CARD} filament and the casp1^{CARD} filament is expected, as such structural complementarity along the helical axis would facilitate recognition between upstream and downstream supramolecular structures (25, 27, 28). For instance, the casp1^{CARD} filament would assemble from either end of the NLRC4^{CARD} filament following the same helical trajectory (3.6 subunit per helical turn, ~4 subunits at the base of both filaments) (Fig. 2*E*). However, it is not clear why NAIP and NLRC4 co-assemble into an 11- to 12-membered split washer-like structure (20–24) to assemble a filament that entails a tetrameric signaling interface (Figs. 1*B* and 2*E*). Also of note, the helical symmetry of the NLRC4^{CARD} filament (left-handed helix) is different from the rest of the assembly (mostly right-handed helix) (23, 24). On the other hand, it is noteworthy that a CARD tetramer resulting from the dimerization of retinoic acid–inducible gene-I (RIG-I) is sufficient to induce the polymerization of downstream MAVS (each RIG-I contains two CARDs in tandem, RIG-I^{2CARD}) (25, 29). Thus, in principle, tetramerization of upstream receptor with a single CARD should be sufficient for assembling a signal-competent complex, yet NLRC4 assembles into an (un)decamer (20–24).

In other inflammasomes that signal through ASC, the recognition between upstream and downstream PYD filaments is also based on their congruent architecture (16, 28). For instance, the filaments assembled by the PYDs of AIM2 and ASC (AIM2^{PYD} and ASC^{PYD}) display the same helical symmetry (*e.g.* 6 subunits at the helical base with C3 symmetry) (16, 28). Using Monte Carlo simulation, we previously demonstrated that dsDNA length, akin to the number of bound AIM2

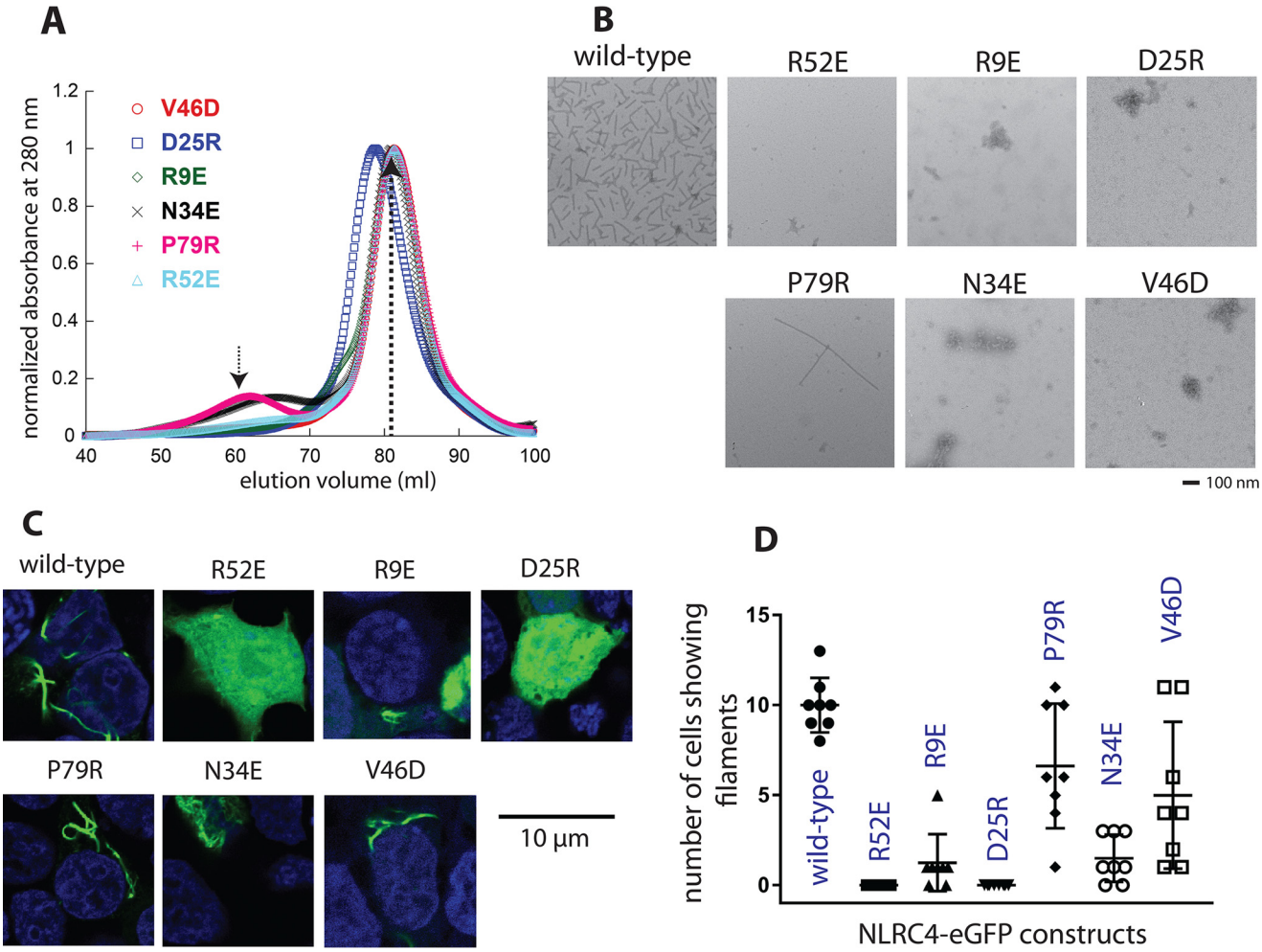

Figure 4. Testing the energetic contribution of surface side-chains of the NLRC4^{CARD} filament. *A*, SEC profiles of NLRC4^{CARD}-eGFP mutants (Superdex 200 16/600). The *dotted arrows* indicate expected elution peak volumes from WT (see also Fig. 1*D*). *B*, negative stain electron micrographs of NLRC4^{CARD}-eGFP variants. The WT image from Fig. 1*E* is shown for comparison. *C*, confocal microscope images HEK293T cells transfected with various NLRC4^{CARD}-eGFP variants. *D*, summary of confocal imaging studies (number of cells showing NLRC4^{CARD}-eGFP filaments per eight random fields, 20× objective zoom). *Error bar* indicates standard deviation.

molecules per duplex, regulates the probability of assembling the hexameric base of the AIM2^{PYD} filament (17). A key phenotype of this assembly mechanism is that both self-assembly and signaling activity of AIM2 nonlinearly increase with the length of dsDNA up to where it would provide the maximal probability for assembling the hexameric base (>200 bp, ~20 AIM2 molecules per duplex) (17, 28, 30). Unlike the AIM2^{PYD}·ASC^{PYD} complex, the recognition between the NLRC4^{CARD}·casp1^{CARD} complex occurs via a tetrameric interface (Fig. 2*E*, *top* and *bottom* views). We thus hypothesized that a possible reason why NLRC4 assembles into an (un)decamer is to maximize the probability of assembling the tetrameric base of its CARD filament. Of note, the linker between the CARD and the rest of NLRC4 will introduce some degree of freedom even when the CARDs are placed in proximity (~12 amino acids). Moreover, each CARD has six protein-protein interaction surfaces instead of one or two well-defined tetrameric interfaces. Thus, simple tetramerization of NLRC4 might not be sufficient to arrange the CARDs in a correct architecture.

To test our hypothesis, we conducted a Monte Carlo simulation that determines the probability of contiguously positioning four CARD protomers on a filament with a tetrameric base (Fig. 5*A*). First, we created a butterflied view of an empty shell that represented the NLRC4^{CARD} filament (each side was still connected in the simulation). We then randomly placed NLRC4^{CARD} protomers to fill the shell, with the stipulation that subsequent protomers must contact existing ones via one of the six protein-protein interaction surfaces. We then monitored the number of protomers required to contiguously fill two, three, and four lateral positions along the helical axis. Here, our simulation results suggested that there was only 5% chance for creating the intact tetrameric base with four available protomers, and the probabilities of aligning two and three protomers along the helical axis were 100 and 50%, respectively (Fig. 5*B*). By contrast, with 11 available protomers, the probability of filling the four lateral positions (*i.e.* creating a tetrameric interface) was nearly 90%. These results explain why simple tetramerization of NLRC4 might not be sufficient to assemble its CARD filament. Moreover, our simulation results provide a rationale for why an oligomer composed of 10 to 11 NLRC4 molecules can be ideal for generating a cognate signaling interface for downstream caspase-1.

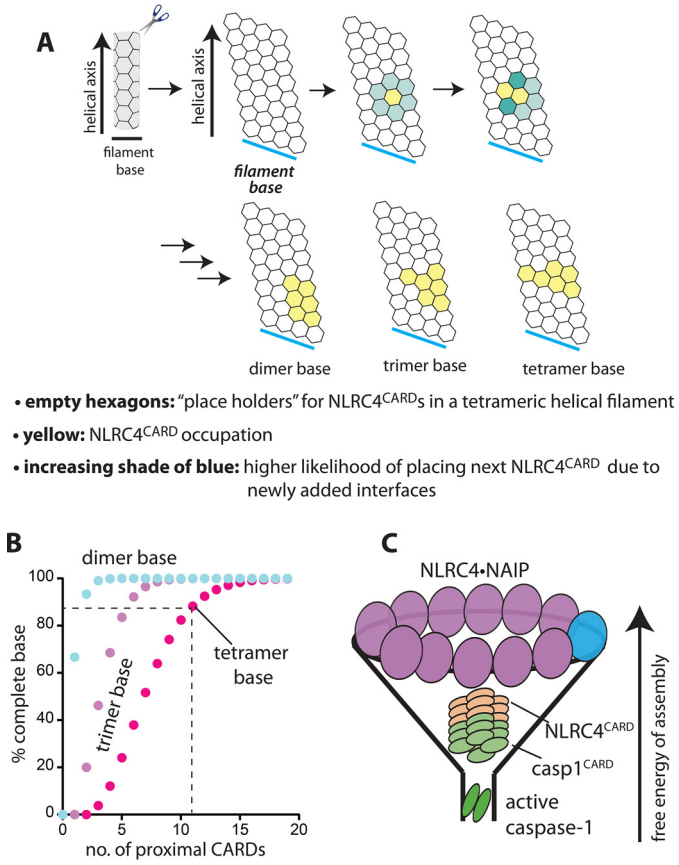

Figure 5. The higher-order split washer–like assembly of NLRC4 maximizes the probability of forming the tetrameric base of its CARD filament. *A*, a scheme describing the Monte Carlo simulation for the NLRC4^{CARD} filament assembly. The filament shell is shown as a butterflied view. In the simulation, the horizontal sides are still connected and the length of the shell is infinite. Each *arrow* indicates stepwise progression of the simulation (*i.e.* individual CARD protomers are added sequentially). *B*, a plot of the probability of base assembly (2, 3, and 4 subunits per intact base) *versus* available proximal NLRC4^{CARD} molecules. *C*, a funnel-like assembly of inflammasome signaling platforms.

Discussion

Inflammasomes are essential for host innate defense against pathogen infection, and are also implicated in cancer formation and auto-inflammatory responses (1, 10, 12). The NAIP·NLRC4 complex represents a unique axis in inflammasome pathways as it directly signals through caspase-1 without ASC. Although there are multiple high-resolution structures of the NAIP·NLRC4 complex, that of the CARD oligomer has been absent. Here, we provide the cryo-EM structure of the NLRC4^{CARD} filament at 3.4 Å resolution, providing the last missing high-resolution piece of the holo-complex. Of note, while our study was under review, Li *et al.* (31) reported a cryo-EM structure of the NLRC4^{CARD} filament at 3.6 Å resolution. Our reconstruction and that of Li *et al.* are essentially identical with the same helical parameters (root mean square deviation = 0.6 Å; rise, 5 Å *versus* 4.9 Å; rotation, 100.6° *versus* 100.5°), further supporting the biological relevance of the present study (31). Combined, here we address two key issues in understanding the signaling mechanisms of inflammasomes: What is the structural framework for the recognition between NLRC4 and caspase-1 and, why is the split washer-like assembly composed of 10 to 11 NLRC4 subunits necessary to assemble the CARD filament?

The structural framework for the signal transduction of the NAIP·NLRC4 inflammasome

A unique aspect of inflammasome pathways is that signal is transduced by the sequential assembly of filamentous oligomers, instead of more ubiquitously found enzyme-mediated chemical reactions (16, 27). In enzymatic cascades, a specific motif at the target/active site or a remote docking site allows the recognition between upstream and downstream signaling partners (32–34). Whether the recognition occurs via the active sites or exo-sites, local structural complementarity is critical for distinguishing cognate partners from others (*i.e.* lock and key) (32–34). It has become increasingly apparent that shape complementarity is also important for signal transduction by supramolecular platforms, only at a larger scale (16, 25–28, 35). For instance, we reported previously that the helical architecture of the upstream AIM2^{PYD} filament is consistent with that of the downstream ASC^{PYD} filament (28). Moreover, the helical architecture of the upstream RIG-I^{2CARD} tetramer is also identical to that of the downstream MAVS^{CARD} filament (25), and such a shape complementarity is also evident in the assembly of PIDDosome (p53-induced protein containing death domain) (35). Our cryo-EM structure of NLRC4^{CARD} further underscores that architectural complementarity underpins the recognition between supramolecular signaling platforms.

Despite the large divergence in primary sequences (*e.g.* Fig. 3*D*), the NLRC4^{CARD} filament shares the common helical architecture with all other known CARD filaments: ~4 subunits per helical turn, left-handed one-start helix with ~100 ± 0.1° twist and 5.0 ± 0.1 Å rise (18, 25, 26). Moreover, all CARDs share very high structural similarity (*e.g.* Fig. 3*C*), the same six interfaces are utilized in the same manner in the filament assembly, and each subunit does not undergo any significant conformational change upon oligomerization (18, 25, 26). Additionally, it appears that similar side-chain interactions are utilized in each interface (Fig. 3*D*) (18, 25, 26). Nevertheless, these filaments do not cross-interact and exclusively signal through their cognate partners (18, 25–27). Future studies will illuminate how homologous filaments recognize and distinguish their cognate and noncognate signaling partners.

(Un)decamerization of NLRC4 and signal funneling by assembly

In inflammasomes that employ the ASC hub, upstream receptors can assemble into infinitely long filaments (*e.g.* AIM2) (16, 28). However, the signal transmission occurs along the helical axis between upstream and downstream assemblies (*i.e.* perpendicular filament base to the helical axis) (16, 28). Previously, we found that dsDNA long enough to accommodate at least 20 AIM2 molecules maximizes the probability of assembling the hexameric filament base ideal for the recognition of ASC (17). Here, our structure shows that even though NLRC4 assembles into an (un)decamer, the signal transduction to caspase-1 occurs via a tetrameric interface between two CARD filaments. Of note, our Monte Carlo simulation suggests that the assembly of the tetrameric base can be maximized by 10

or more proximal protomers. Our results provide an explanation for why the (un)decamerization of NLRC4 would be ideal for signal propagation. On the other hand, the final step in all inflammasome pathways is the dimerization of caspase-1 (1, 18), again requiring a lower-order oligomeric signaling interface than the tetrameric interface between CARD filaments. Thus, it appears that the oligomeric states required to carry out each signaling step progressively decrease in inflammasome cascades. Together, considering that kinetic and thermodynamic barriers would be greater for assembling higher-order suprastructures than lower-order assemblies, it is tempting to speculate that such a strategy would allow inflammasomes to maximize their signaling fidelity and efficiency in a funnel-like manner (Fig. 5*C*).

Experimental procedures

Protein expression and purification

WT and mutant human NLRC4^{CARD} constructs (amino acids 1–96) were cloned into either unmodified pET21b vector or a pET21b containing an N-terminal MBP followed by a recognition site for the TEVp and C-terminal eGFP. Resulting NLRC4^{CARD} constructs were transformed into *Escherichia coli* BL21 Rosetta2^{DE3} cells and protein expression was induced using 200 μM isopropyl 1-thio-β-D-galactopyranoside at 18 °C for 16–18 h. The cells were lysed by sonication in 25 mM $NaPO_4$, 400 mM NaCl, 40 mM imidazole, and 8 mM β-mercaptoethanol at pH 8. NLRC4^{CARD} constructs were then purified by nickel-nitrilotriacetic acid chromatography via a C-terminal His_6-tag followed by SEC. Proteins were stored in 20 mM HEPES at pH 7.4, 400 mM NaCl, 10% glycerol, 1 mM EDTA, and 1 mM DTT and frozen at −80 °C.

Negative stain EM

Samples were diluted to 750 nM into a buffer containing 40 mM HEPES, 160 mM NaCl, 1 mM EDTA, 5 mM DTT, at pH 7. To induce polymerization, 3 μM TEVp was added to each sample and incubated for 1.5 h at room temperature (24 ± 2 °C). nsEM imaging experiments were performed using glow-discharged carbon-coated copper grids and 0.75% uranyl formate staining solution as described previously (17, 28).

Cryo-EM sample preparation

5 μl sample was applied to Lacey grids, followed by automatically blotting for 1.5 s and plunge freezing using the FEI Vitrobot Mark IV operated at 100% humidity and room temperature (Johns Hopkins University). Cryo-EM data were collected at the National Cancer Institute National cryo-EM facility (NCI NCEF, Frederick, MD) using the FEI Titan equipped with the Gatan K2 direct electron detector operating at 300 keV using the super-resolution mode (0.66 Å/pixel). A total of 1,690 micrographs were collected from one grid at a defocus range from −1.0 to −2.5 μm. Each micrograph was equally fractioned into 40 frames with a total exposure time of 15 s and a total dose of ~40 electrons/Å^2.

Helical reconstruction and model building

The 1,690 micrographs were binned by two sections (to 1.32 Å/pixel) and frames were aligned using MotionCor2 (36). The defocus values and astigmatism of the micrographs were determined by CTFFIND3 for the aligned full-dose micrographs (37). A total of 1,486 micrographs were selected (images with good contrast transfer function (CTF) determination and defocus <3 μm) for subsequent image processing. CTF was corrected by multiplying the micrographs (only first 20 frames were aligned with a total dose of ~20 electrons/Å^2) with the theoretical CTF, which both corrects the phases and improves the signal-to-noise ratio. The e2helixboxer program in EMAN2 software package (38) was used for boxing long filaments from the full-dose images. The CTF-corrected micrographs were used for the segment extraction, with a total of 402,078 384-pixel-long overlapping segments (with a shift of 1.5 times of axial rise) generated. The SPIDER software package (39) was used for subsequent processing and reconstruction. Using a featureless cylinder as an initial reference, 299,537 segments were used in IHRSR program for the final reconstruction after the helical parameters (a rotation of 100.6° and an axial rise of 5.0 Å per subunit) converged. The resolution of the final reconstruction was estimated by the Fourier Shell Correlation (FSC) between two independent half maps, which shows 3.4 Å at FSC = 0.143.

We used the crystal structure of a homologous protein CARD8 (PDB ID: 4IKM) (40) as an initial template to dock into the NLRC4 cryo-EM map by rigid body fitting, and then manually edited the model in Chimera (41) and Coot (42). We then used the modified model as the starting template to further refine against the segmented cryo-EM map using RosettaCM using default values (43). The refined monomeric model of NLRC4 was then rebuilt by RosettaCM with helical symmetry and real-space refined using Phenix (44) to improve the stereochemistry as well as the model-map correlation coefficient. The NLRC4 model was validated with MolProbity (45) and the coordinates deposited to the Protein Data Bank with the accession code 6MKS. The corresponding cryo-EM map was deposited in the EMDB with accession code EMD-9137.

Confocal microscopy

NLRC4^{CARD}-eGFP variants were cloned into pCMV6 vector. Plasmids were then transiently transfected into HEK293T cells using Lipofectamine (Invitrogen). Cells were fixed with 4% paraformaldehyde, permeabilized in acetone, and mounted on glass slides using ProLong Gold Antifade Mountant with DAPI (Thermo Fisher). Cells were imaged using a Zeiss Axioskop 50 with a Zeiss Axiocam HRC camera and an Axio Observer inverted microscope with LSM700 confocal module.

Monte Carlo simulation

The overall strategy is based on our previously published protocol (17), with specific modifications for NLRC4^{CARD} architecture. The code has been rewritten in Rust and is available at https://gitlab.com/matyszm/pydnode-nlrc4 (commit 7f17c4db was used to generate the values present in the paper)[5]. Each point is an average of 1,000,000 runs.

[5] Please note that the JBC is not responsible for the long-term archiving and maintenance of this site or any other third party hosted site.

Author contributions—M. M. and W. Z. software; M. M., E. H. E., and J. S. validation; M. M., W. Z., J. L., B. A., and J. S. investigation; M. M., W. Z., and J. S. writing-original draft; M. M., W. Z., J. L., and E. H. E. writing-review and editing; B. A. data curation; B. A. methodology; E. H. E. and J. S. supervision; E. H. E. and J. S. project administration; J. S. conceptualization; J. S. formal analysis; J. S. funding acquisition.

Acknowledgments—We thank the Sohn lab members for discussion and the staff at NCI NCEF for cryo-EM data collection. The Johns Hopkins Microscope Facility was supported by National Institutes of Health Grant S10 OD016734.

References

1. Guo, H., Callaway, J. B., and Ting, J. P. (2015) Inflammasomes: Mechanism of action, role in disease, and therapeutics. *Nat. Med.* **21,** 677–687 CrossRef Medline
2. Thornberry, N. A., Bull, H. G., Calaycay, J. R., Chapman, K. T., Howard, A. D., Kostura, M. J., Miller, D. K., Molineaux, S. M., Weidner, J. R., and Aunins, J. (1992) A novel heterodimeric cysteine protease is required for interleukin-1β processing in monocytes. *Nature* **356,** 768–774 CrossRef Medline
3. Liu, X., Zhang, Z., Ruan, J., Pan, Y., Magupalli, V. G., Wu, H., and Lieberman, J. (2016) Inflammasome-activated gasdermin D causes pyroptosis by forming membrane pores. *Nature* **535,** 153–158 CrossRef Medline
4. Bandera, A., Masetti, M., Fabbiani, M., Biasin, M., Muscatello, A., Squillace, N., Clerici, M., Gori, A., and Trabattoni, D. (2018) The NLRP3 inflammasome is upregulated in HIV-infected antiretroviral therapy-treated individuals with defective immune recovery. *Front. Immunol.* **9,** 214 CrossRef Medline
5. Maruzuru, Y., Ichinohe, T., Sato, R., Miyake, K., Okano, T., Suzuki, T., Koshiba, T., Koyanagi, N., Tsuda, S., Watanabe, M., Arii, J., Kato, A., and Kawaguchi, Y. (2018) Herpes simplex virus 1 VP22 inhibits AIM2-dependent inflammasome activation to enable efficient viral replication. *Cell Host Microbe* **23,** 254–265.e257 CrossRef Medline
6. Kim, S., Bauernfeind, F., Ablasser, A., Hartmann, G., Fitzgerald, K. A., Latz, E., and Hornung, V. (2010) *Listeria monocytogenes* is sensed by the NLRP3 and AIM2 inflammasome. *Eur. J. Immunol.* **40,** 1545–1551 CrossRef Medline
7. Reyes Ruiz, V. M., Ramirez, J., Naseer, N., Palacio, N. M., Siddarthan, I. J., Yan, B. M., Boyer, M. A., Pensinger, D. A., Sauer, J. D., and Shin, S. (2017) Broad detection of bacterial type III secretion system and flagellin proteins by the human NAIP/NLRC4 inflammasome. *Proc. Natl. Acad. Sci. U.S.A.* **114,** 13242–13247 CrossRef Medline
8. Fernandes-Alnemri, T., Yu, J. W., Juliana, C., Solorzano, L., Kang, S., Wu, J., Datta, P., McCormick, M., Huang, L., McDermott, E., Eisenlohr, L., Landel, C. P., and Alnemri, E. S. (2010) The AIM2 inflammasome is critical for innate immunity to *Francisella tularensis*. *Nat. Immunol.* **11,** 385–393 CrossRef Medline
9. Yang, C. A., and Chiang, B. L. (2015) Inflammasomes and human autoimmunity: A comprehensive review. *J. Autoimmun.* **61,** 1–8 CrossRef Medline
10. Yi, Y. S. (2018) Role of inflammasomes in inflammatory autoimmune rheumatic diseases. *Korean J Physiol. Pharmacol.* **22,** 1–15 CrossRef Medline
11. Lee, S., Nakahira, K., Dalli, J., Siempos, I. I., Norris, P. C., Colas, R. A., Moon, J. S., Shinohara, M., Hisata, S., Howrylak, J. A., Suh, G. Y., Ryter, S. W., Serhan, C. N., and Choi, A. M. K. (2017) NLRP3 inflammasome deficiency protects against microbial sepsis via increased lipoxin B4 synthesis. *Am. J. Respir. Crit. Care Med.* **196,** 713–726 CrossRef Medline
12. Henao-Mejia, J., Elinav, E., Thaiss, C. A., and Flavell, R. A. (2014) Inflammasomes and metabolic disease. *Annu. Rev. Physiol.* **76,** 57–78 CrossRef Medline
13. De Nardo, D., and Latz, E. (2011) NLRP3 inflammasomes link inflammation and metabolic disease. *Trends Immunol.* **32,** 373–379 CrossRef Medline
14. Man, S. M., Karki, R., and Kanneganti, T. D. (2016) AIM2 inflammasome in infection, cancer, and autoimmunity: Role in DNA sensing, inflammation, and innate immunity. *Eur. J. Immunol.* **46,** 269–280 CrossRef Medline
15. Lin, C., and Zhang, J. (2017) Inflammasomes in inflammation-induced cancer. *Front Immunol.* **8,** 271 CrossRef Medline
16. Lu, A., Magupalli, V. G., Ruan, J., Yin, Q., Atianand, M. K., Vos, M. R., Schröder, G. F., Fitzgerald, K. A., Wu, H., and Egelman, E. H. (2014) Unified polymerization mechanism for the assembly of ASC-dependent inflammasomes. *Cell* **156,** 1193–1206 CrossRef Medline
17. Matyszewski, M., Morrone, S. R., and Sohn, J. (2018) Digital signaling network drives the assembly of the AIM2-ASC inflammasome. *Proc. Natl. Acad. Sci. U.S.A.* **115,** E1963–E1972 CrossRef Medline
18. Lu, A., Li, Y., Schmidt, F. I., Yin, Q., Chen, S., Fu, T. M., Tong, A. B., Ploegh, H. L., Mao, Y., and Wu, H. (2016) Molecular basis of caspase-1 polymerization and its inhibition by a new capping mechanism. *Nat. Struct. Mol. Biol.* **23,** 416–425 CrossRef Medline
19. Vance, R. E. (2015) The NAIP/NLRC4 inflammasomes. *Curr. Opin. Immunol.* **32,** 84–89 CrossRef Medline
20. Hu, Z., Yan, C., Liu, P., Huang, Z., Ma, R., Zhang, C., Wang, R., Zhang, Y., Martinon, F., Miao, D., Deng, H., Wang, J., Chang, J., and Chai, J. (2013) Crystal structure of NLRC4 reveals its autoinhibition mechanism. *Science* **341,** 172–175 CrossRef Medline
21. Hu, Z., Zhou, Q., Zhang, C., Fan, S., Cheng, W., Zhao, Y., Shao, F., Wang, H. W., Sui, S. F., and Chai, J. (2015) Structural and biochemical basis for induced self-propagation of NLRC4. *Science* **350,** 399–404 CrossRef Medline
22. Zhang, L., Chen, S., Ruan, J., Wu, J., Tong, A. B., Yin, Q., Li, Y., David, L., Lu, A., Wang, W. L., Marks, C., Ouyang, Q., Zhang, X., Mao, Y., and Wu, H. (2015) Cryo-EM structure of the activated NAIP2-NLRC4 inflammasome reveals nucleated polymerization. *Science* **350,** 404–409 CrossRef Medline
23. Tenthorey, J. L., Haloupek, N., López-Blanco, J. R., Grob, P., Adamson, E., Hartenian, E., Lind, N. A., Bourgeois, N. M., Chacón, P., Nogales, E., and Vance, R. E. (2017) The structural basis of flagellin detection by NAIP5: A strategy to limit pathogen immune evasion. *Science* **358,** 888–893 CrossRef Medline
24. Diebolder, C. A., Halff, E. F., Koster, A. J., Huizinga, E. G., and Koning, R. I. (2015) Cryoelectron tomography of the NAIP5/NLRC4 inflammasome: Implications for NLR activation. *Structure* **23,** 2349–2357 CrossRef Medline
25. Wu, B., Peisley, A., Tetrault, D., Li, Z., Egelman, E. H., Magor, K. E., Walz, T., Penczek, P. A., and Hur, S. (2014) Molecular imprinting as a signal-activation mechanism of the viral RNA sensor RIG-I. *Mol. Cell* **55,** 511–523 CrossRef Medline
26. David, L., Li, Y., Ma, J., Garner, E., Zhang, X., and Wu, H. (2018) Assembly mechanism of the CARMA1-BCL10-MALT1-TRAF6 signalosome. *Proc. Natl. Acad. Sci. U.S.A.* **115,** 1499–1504 CrossRef Medline
27. Kagan, J. C., Magupalli, V. G., and Wu, H. (2014) SMOCs: Supramolecular organizing centres that control innate immunity. *Nat. Rev. Immunol.* **14,** 821–826 CrossRef Medline
28. Morrone, S. R., Matyszewski, M., Yu, X., Delannoy, M., Egelman, E. H., and Sohn, J. (2015) Assembly driven activation of the AIM2 foreign-dsDNA sensor provides a polymerization template for downstream ASC. *Nat. Commun.* **6,** 7827 CrossRef Medline
29. Peisley, A., Wu, B., Xu, H., Chen, Z. J., and Hur, S. (2014) Structural basis for ubiquitin-mediated antiviral signal activation by RIG-I. *Nature* **509,** 110–114 CrossRef Medline
30. Roberts, T. L., Idris, A., Dunn, J. A., Kelly, G. M., Burnton, C. M., Hodgson, S., Hardy, L. L., Garceau, V., Sweet, M. J., Ross, I. L., Hume, D. A., and Stacey, K. J. (2009) HIN-200 proteins regulate caspase activation in response to foreign cytoplasmic DNA. *Science* **323,** 1057–1060 CrossRef Medline
31. Li, Y., Fu, T. M., Lu, A., Witt, K., Ruan, J., Shen, C., and Wu, H. (2018) Cryo-EM structures of ASC and NLRC4 CARD filaments reveal a unified

mechanism of nucleation and activation of caspase-1. *Proc. Natl. Acad. Sci. U.S.A.* **115,** 10845–10852 CrossRef Medline

32. Sohn, J., Kristjánsdóttir, K., Safi, A., Parker, B., Kiburz, B., and Rudolph, J. (2004) Remote hot spots mediate protein substrate recognition for the Cdc25 phosphatase. *Proc. Natl. Acad. Sci. U.S.A.* **101,** 16437–16441 CrossRef Medline
33. Schulman, B. A., Lindstrom, D. L., and Harlow, E. (1998) Substrate recruitment to cyclin-dependent kinase 2 by a multipurpose docking site on cyclin A. *Proc. Natl. Acad. Sci. U.S.A.* **95,** 10453–10458 CrossRef Medline
34. Li, J., and Yuan, J. (2008) Caspases in apoptosis and beyond. *Oncogene* **27,** 6194–6206 CrossRef Medline
35. Park, H. H., Logette, E., Raunser, S., Cuenin, S., Walz, T., Tschopp, J., and Wu, H. (2007) Death domain assembly mechanism revealed by crystal structure of the oligomeric PIDDosome core complex. *Cell* **128,** 533–546 CrossRef Medline
36. Zheng, S. Q., Palovcak, E., Armache, J. P., Verba, K. A., Cheng, Y., and Agard, D. A. (2017) MotionCor2: Anisotropic correction of beam-induced motion for improved cryo-electron microscopy. *Nat. Methods* **14,** 331–332 CrossRef Medline
37. Mindell, J. A., and Grigorieff, N. (2003) Accurate determination of local defocus and specimen tilt in electron microscopy. *J. Struct. Biol.* **142,** 334–347 CrossRef Medline
38. Tang, G., Peng, L., Baldwin, P. R., Mann, D. S., Jiang, W., Rees, I., and Ludtke, S. J. (2007) EMAN2: An extensible image processing suite for electron microscopy. *J. Struct. Biol.* **157,** 38–46 CrossRef Medline
39. Frank, J., Radermacher, M., Penczek, P., Zhu, J., Li, Y., Ladjadj, M., and Leith, A. (1996) SPIDER and WEB: Processing and visualization of images in 3D electron microscopy and related fields. *J. Struct. Biol.* **116,** 190–199 CrossRef Medline
40. Jin, T., Huang, M., Smith, P., Jiang, J., and Xiao, T. S. (2013) The structure of the CARD8 caspase-recruitment domain suggests its association with the FIIND domain and procaspases through adjacent surfaces. *Acta Crystallogr. Sect. F Struct. Biol. Cryst. Commun.* **69,** 482–487 CrossRef Medline
41. Pettersen, E. F., Goddard, T. D., Huang, C. C., Couch, G. S., Greenblatt, D. M., Meng, E. C., and Ferrin, T. E. (2004) UCSF Chimera—a visualization system for exploratory research and analysis. *J. Comput. Chem.* **25,** 1605–1612 CrossRef Medline
42. Emsley, P., Lohkamp, B., Scott, W. G., and Cowtan, K. (2010) Features and development of Coot. *Acta Crystallogr. D Biol. Crystallogr.* **66,** 486–501 CrossRef Medline
43. Wang, R. Y., Song, Y., Barad, B. A., Cheng, Y., Fraser, J. S., and DiMaio, F. (2016) Automated structure refinement of macromolecular assemblies from cryo-EM maps using Rosetta. *Elife* **5,** e17219 CrossRef Medline
44. Adams, P. D., Afonine, P. V., Bunkóczi, G., Chen, V. B., Davis, I. W., Echols, N., Headd, J. J., Hung, L. W., Kapral, G. J., Grosse-Kunstleve, R. W., McCoy, A. J., Moriarty, N. W., Oeffner, R., Read, R. J., Richardson, D. C., Richardson, J. S., Terwilliger, T. C., and Zwart, P. H. (2010) PHENIX: A comprehensive Python-based system for macromolecular structure solution. *Acta Crystallogr. D Biol. Crystallogr.* **66,** 213–221 CrossRef Medline
45. Chen, V. B., Arendall, W. B., 3rd, Headd, J. J., Keedy, D. A., Immormino, R. M., Kapral, G. J., Murray, L. W., Richardson, J. S., and Richardson, D. C. (2010) MolProbity: All-atom structure validation for macromolecular crystallography. *Acta Crystallogr. D Biol. Crystallogr.* **66,** 12–21 CrossRef Medline